Rotor-Obstacle Aerodynamic Interaction in Hovering Flight: An Experimental Survey.

Daniele Zagaglia
Ph.D. Candidate
Politecnico di Milano
Dipartimento di Scienze e Tecnologie Aerospaziali
Via La Masa 34, 20156 Milano, Italy

Michea Giuni
Research Assistant
University of Glasgow
Aerospace Sciences Division, School of Engineering
James Watt Building South, Glasgow G12 8QQ, UK

Richard B. Green
Senior Lecturer
University of Glasgow
Aerospace Sciences Division, School of Engineering
James Watt Building South, Glasgow G12 8QQ, UK

ABSTRACT

Despite the presence of a fair number of numerical and experimental works on the rotor-obstacle interaction, a systematic study of the aerodynamic phenomena involved is lacking. In this paper a comprehensive experimental survey carried out at University of Glasgow is described, taking advantage of two different rotor rigs and several experimental techniques. Load measurements on the rotor were carried out in order to assess the rotor performance for different positions with respect to a cubic obstacle, thus simulating a set of possible hovering flight conditions around the obstacle. Laser Doppler Anemometry (LDA) measurements of the rotor inflow were used in order to investigate how the aerodynamic interaction affected the rotor performance. Eventually Stereoscopic Particle Image Velocimetry (SPIV) measurements in the region between the rotor and the obstacle were carried out in order to have a better insight of the interacting flow field.

NOTATION

A	Rotor disc area
c	Blade chord
c_T	Thrust Coefficient, $T/\left(\rho V_{\text{TIP}}^2 A\right)$
c_Q	Torque Coefficient, $Q/\left(\rho V_{\text{TIP}}^2 AR\right)$
c_{Mx}	$x-$ Moment Coefficient, $M_x/\left(\rho V_{\text{TIP}}^2 AR\right)$
c_{My}	$y-$ Moment Coefficient, $M_y/\left(\rho V_{\text{TIP}}^2 AR\right)$
CIRA	Italian Aerospace Centre
D	Rotor disc diameter
DLR	German Aerospace Centre
FM	Figure of Merit, $c_T^{3/2}/(\sqrt{2}c_Q)$
IGE	In Ground Effect condition
L	Cubic obstacle size
LDA	Laser Doppler Anemometry
M	PIV optical magnification factor
N_b	Number of blades
NLR	Dutch Aerospace Centre
OGE	Out of Ground Effect condition
ONERA	French Aerospace Centre
PIV	Particle Image Velocimetry
R	Rotor disc radius
SPIV	Stereoscopic Particle Image Velocimetry
v	Out-of-plane velocity component
(X,Y,Z)	Absolute reference system
(x,y,z)	Rotor reference system
Δt	Time delay between two laser pulses
ε_u	Uncertainty on the in-plane velocity components
$\varepsilon_{u,\text{op}}$	Uncertainty on the out-of-plane velocity component
ρ	Air density
σ	Rotor Solidity, defined as $N_b c/(\pi R)$
θ	Camera separation semi-angle
θ_c	Collective Pitch angle
Ω	Rotor rotational frequency

Presented at the AHS 72nd Annual Forum, West Palm Beach, Florida, May 17–19, 2016.

INTRODUCTION

Helicopters, due to their capability of managing hovering flight, are highly exploited in missions within confined areas. The aerodynamic interaction between the rotor-induced wake and the surrounding obstacles generates, on the one hand, high compensatory workload for the pilot and degradation of aircraft performance, on the other hand unsteady forces which can stress the structure of the obstacle. A few experimental and numerical investigations have been produced on this topic in the last few years, especially for the Dynamic Interface problem (Ref. 1), where the helicopter interacts with the superstructures which are usually present on ship decks (see for instance (Ref. 2) and (Ref. 3)). For what

concerns the experimental literature on this topic, a few geometries and configurations were analysed by means of different experimental techniques, such as loads measurements of the helicopter (Ref. 4), velocity measurements in the rotor inflow region and wake (Ref. 5) and Particle Image Velocimetry (Ref. 6). A comprehensive analysis of the performance of a fully-articulated rotor between two vertical walls was achieved by (Ref. 7).

Despite the presence of a fair number of numerical and experimental works, a systematic study of these aerodynamic phenomena is lacking. The GARTEUR Action Group 22 *"Forces on Obstacles in Rotor Wake"*, comprising several universities (Politecnico di Milano, University of Glasgow, University of Liverpool, National Technical university of Athens) and research institutes (CIRA, DLR, ONERA, NLR), originates from the idea of promoting activities which could contribute to a better understanding of these phenomena. In this framework, the production of an experimental database was carried out initially at Politecnico di Milano (Ref. 8), analysing the case of a model helicopter with fuselage interacting with a cuboid obstacle, in absence of wind. Following this first experience, an extended database comprising several measurement points and experimental techniques was produced at University of Glasgow with a deeper insight on the interacting flow, which is the subject of the present paper.

As previously stated a systematic study of the aerodynamic phenomena involved is still lacking. Moreover the past investigations usually either rely on just one measurement technique or they usually involve quite specific geometries (e.g. ships). Therefore the purpose of the present work is to provide an extended experimental database for the rotor-obstacle aerodynamic investigation using a simplified geometry (cubic obstacle) and different kinds of experimental surveys, i.e. load measurements on the rotor, Laser Doppler Anemometry (LDA) in the rotor inflow region and Stereoscopic Particle Image Velocimetry (SPIV) of the the flow-field.

THE EXPERIMENTAL APPARATUS

Test rig description and Test matrix

The experimental campaign was conducted at the University of Glasgow. Two different rotor rigs were employed, whose main features are reported in Table 1. The experimental campaign consisted of a set of tests reproducing hovering flight conditions at different positions with respect to a simplified obstacle with a cubic shape (the measurement points are represented in Figure 1). The measurements were carried out in the symmetry plane of the problem ($Y/R = 0$).

The data that will be presented in this paper follow the conventions of Figure 1 and Figure 2. Two different reference systems are defined: the global reference system (X,Y,Z) which defines the position of the rotor hub centre with respect to the obstacle and the rotor reference system (x,y,z), which corresponds to the load-cell axes. The origin of the absolute (X,Y,Z) coordinate system is fixed and it is placed on the floor, at the obstacle mid-span (as in Figure 2). The LDA

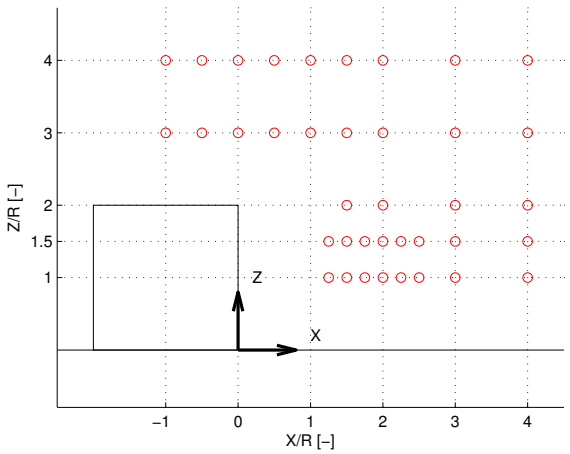

Fig. 1: Measurement points in the problem symmetry plane ($Y/R = 0$). Each red circle represents the position of the rotor hub-centre for the corresponding measurement.

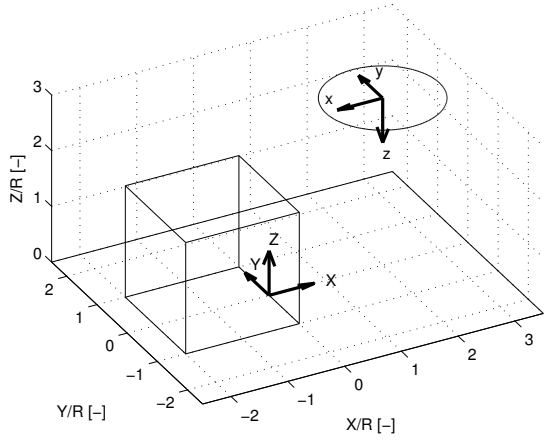

Fig. 2: Absolute and Rotor reference systems.

measurements are defined in the rotor system too. Hence, according to this convention, a positive induced velocity points downwards.

The Large rotor rig was instrumented with a 6-components load cell, so that the forces and the moments on the rotor could be monitored. LDA measurements along the rotor x and y axes (see the Reference system of Figure 2), 4 cm $(4\%D)$ above the rotor plane, were performed in order to understand how the interacting flow field affected the rotor performance. The LDA measurement were carried out in a subset of the measurement points of figure 1, i.e. those at $Z/R = 1.5, 2, 3$, due to the maximum and minimum height achievable by the traversing system. Eventually a Stereo-PIV campaign was carried out on the "Wee" rotor rig in order to disclose the main features of the interacting flow field in a few relevant configurations.

The Experimental setup and procedure

As previously stated, the Large rotor rig was instrumented with a 6-components load cell which allowed the measure-

Characteristics	Symbol	Large rotor rig	"Wee" rotor rig
Cubic Obstacle size	L	1 m	0.3 m
Diameter	D	1 m	0.3 m
Number of blades	N_b	4	2
Blade chord	c	53 mm	31.7 mm
Solidity	σ	0.135	0.134
Collective pitch	θ_c	8°	8°
Rotor Rotational frequency	Ω	1200 RPM (20 Hz)	4000 RPM (66.6 Hz)
Reynolds Number at blade tip	Re_{TIP}	220000	132000
Mach Number at blade tip	M_{TIP}	0.18	0.18
Type of Experimental investigation		Loads measurement, LDA	Stereo-PIV

Table 1: Main features of the Rotor Rigs

ments of the forces and moments generated by the rotor. The employed load cell was an AMTI MC36, whose amplifier was set at a very high frequency so that it would respond to the forces and moments. The nominal accuracy of the load cell was 0.25% of the full-scale output, corresponding approximately to 0.5% of the measured thrust in Out of Ground Effect condition. The actual load measurements were obtained as the average of 5 runs, each of which was 2.5 s long. The reduced acquisition time was driven by the need of reducing the load-cell thermal drift.

The rotor inflow measurements were carried out by means of a Dantec 2D FiberFlow two-component Laser Doppler Anemometry (LDA) system. 112 mm probes with beam expanders allowed measurements from over 2000 mm of distance with a measurement volume ellipsoid dimensions of $2.62 \times 0.12 \times 0.12$ mm^3. Seeding was provided by an oil substrate with particle diameter of $0.2-0.3$ μm. 7500 valid samples were taken at every measurement point, with accuracy of approximately 0.02 m/s corresponding to 0.4% of the maximum inflow velocity. The LDA system was mounted on a 3D traverse system allowing positioning with accuracy of less than 0.1 mm. Every LDA sweep comprised 101 evenly-spaced measurement points along the rotor diameter, allowing a spatial resolution of 10 mm ($1\%D$).

The Stereoscopic PIV was used to investigate the flow in the region between the obstacle and the rotor of the "Wee" rotor rig. These measurements were carried out by means of a LaVision system running Davis 8. The images were acquired by two Phantom v341 cameras, whose resolution was 4Mpixel. The seeded flow was illuminated by a Nd:YAG laser capable of 100mJ pulses at a maximum repetition rate of 200Hz, thus allowing time resolved measurement of the flow field development to be made. However only the ensemble-averaged measurements over 500 image pairs are addressed in the present paper. The cameras, which were placed on either side of the laser sheet, were equipped with Scheimpflug adaptors and an angle separation of around 30 degrees was used. Calibration was performed using a 3D calibration plate and Davis 8 software. Oil based seeding for the PIV system was used with nominal particle diameter less than $1\mu m$. The image pairs were post-processed by means of the Davis 8 software using 32×32 pixels interrogation windows with an overlap factor of 50%. The uncertainty of the velocity measurement was estimated (according to (Ref. 9)) to be $\varepsilon_u = \frac{1}{\sqrt{2}} \frac{0.1}{M\Delta t} = 0.1$ m/s for the in-plane velocity components and $\varepsilon_{u,\mathrm{op}} = \frac{1}{\sqrt{2}\tan\theta} \frac{0.1}{M\Delta t} = 0.33$ m/s for the out-of-plane component, assuming a maximum displacement error of 0.1 pixels since a gaussian sub-pixel interpolation algorithm was used. An optical magnification factor of M =3.4161 pixel/m was used, together with a pulse separation time of $\Delta t = 200$ μs and $\theta = 15^\circ$, corresponding to half of the camera separation angle.

RESULTS

In this section we analyse the main results of the experimental survey. The load measurements for the different rotor position are presented in Fig. 3 (plots) and Fig. 4, the LDA inflow measurements along the x and y axes are presented in Fig. 5 and finally the PIV measurements are presented in Fig. 6 (in-plane velocity magnitude contours and streamlines) and 7 (out-of-plane velocity contours).

A set of load measurements were initially carried out in order to qualify the rotor performance in absence of the obstacle. The rotor was placed as high as possible ($Z/R = 4$) in order to assess the Out-of-Ground-Effect (OGE) condition. A $c_{T,\mathrm{OGE}}$ of $7.36 \cdot 10^{-3}$ and a $c_{Q,\mathrm{OGE}}$ of $8.75 \cdot 10^{-4}$ were obtained, leading to a Figure of Merit of FM_{OGE}=0.51.

Variation of the thrust coefficient with respect to the out-of-ground-effect (OGE) condition is presented in the plots of Figure 3a and 4a. The typical thrust increase (up to 20%) due to the ground effect can be appreciated in both the region over the centre of the obstacle and far from the obstacle, since the relative distance to the closest surface (either the floor or the top of the obstacle) is the same ($1R$) and the rotor projection lies completely on the obstacle top face. However two main regions where the rotor performance deviates from the nominal behaviour can be observed.

The first region is the one above the edge of the obstacle, where the thrust coefficient decreases as the rotor is positioned outwards, owing to the minority of the rotor lying over the upper surface of the obstacle (as already observed in (Ref. 8)). This phenomenon can be appreciated also in the inflow profile

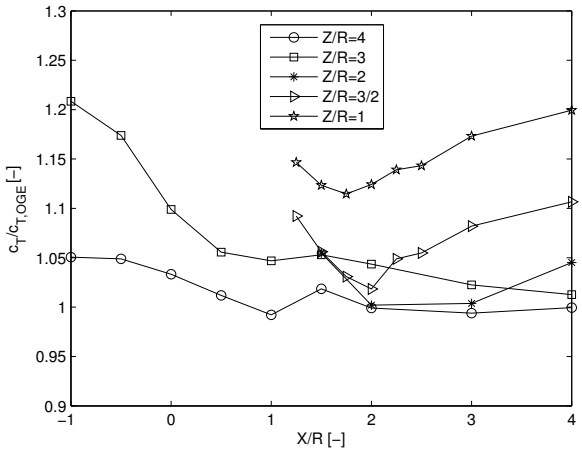

(a) Ratio between the Thrust Coefficient c_T and the one measured in OGE

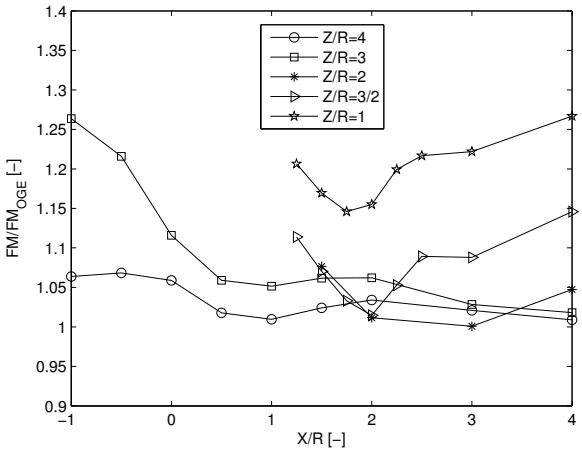

(b) Ratio between the Figure of Merit FM and the one measured in OGE

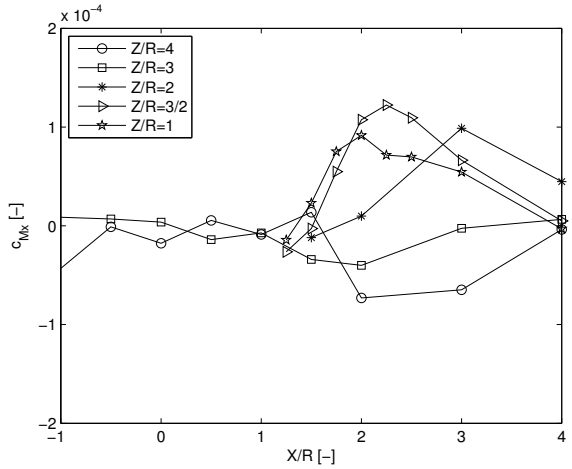

(c) x-moment coefficient

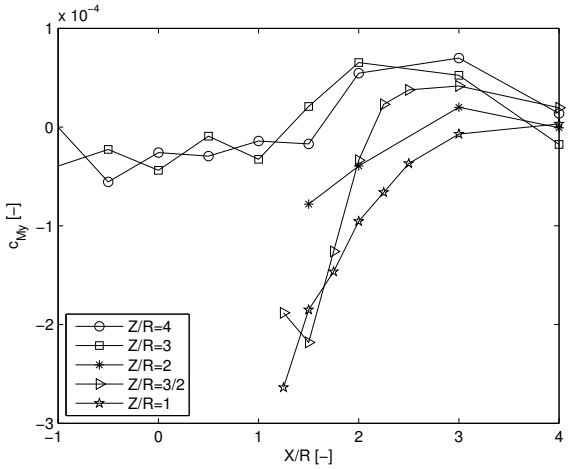

(d) y-moment coefficient

Fig. 3: Loads acting on the rotor vs rotor position

of Figure 5a measured by means of the LDA system. In this case a gradual reduction of the inflow velocity is observed going from $X/R = 1$ to $X/R = -1$, as prescribed by the ground effect. However, one would expect this variation to be non-symmetrical, since only part of the rotor projection lies on the top of the obstacle and thus is affected by the ground effect. Conversely this appears not to be the case since the inflow profile of Fig. 5a is pretty symmetrical. This is also testified by the fact that the the pitch and roll moments of Fig. 3c and 3d are quite close to zero in the region $-1 < X/R < 1$. An additional interesting moment behaviour can be observed moving the rotor away from the obstacle ($1 < X/R < 3$) at the same heights ($Z/R = 3,4$), where a positive $y-$ moment develops on the rotor, which fades out in the outer region ($X/R > 4$).

The second region, probably of more interest, is the one just beside the obstacle ($1 < X/R < 3$, $1 < Z/R < 3$), where a severe ground effect reduction can be observed, since the thrust coefficient drops to a value slightly below the OGE one, even at low heights. This behaviour is caused by the development of a recirculation region caused by the fact that the rotor wake, once deflected by the ground, is deflected again by the obstacle and then re-ingested by the rotor itself. This recirculation region, which is evident in the PIV flow-fields of Figure 6, causes an increased induced velocity and a consequent loss of thrust, similar to a partial vortex ring state. This effect is deeply dependent on both the rotor height and distance from the obstacle. A maximum thrust loss of 8% with respect to the furthest rotor position at the same height can be observed at $Z/R = 1,3/2$, whereas at $Z/R = 2$ the maximum thrust loss is lower (approximately 4 %). Moreover one can appreciate the fact that the thrust loss is not monotonic when getting closer to the obstacle, but it presents a local minimum at approximately $X/R = 2$. This can be explained looking at Fig. 6, where at $X/R = 2$ (Fig.6d, 6e, 6f) the in-plane velocity on the edge of the obstacle (the green layer) is higher than in the other cases (approximately 4 m/s instead of 2.5), thus implying a

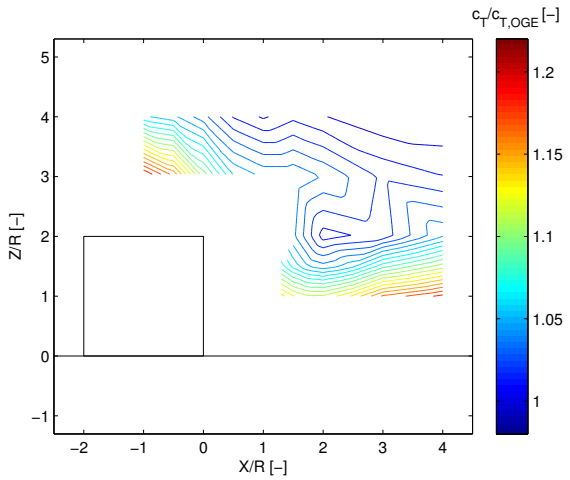

(a) Ratio between the Thrust Coefficient c_T and the one measured in OGE

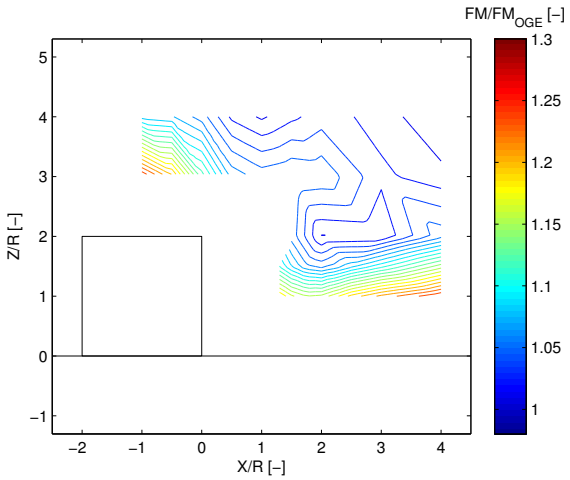

(b) Ratio between the Figure of Merit FM and the one measured in OGE

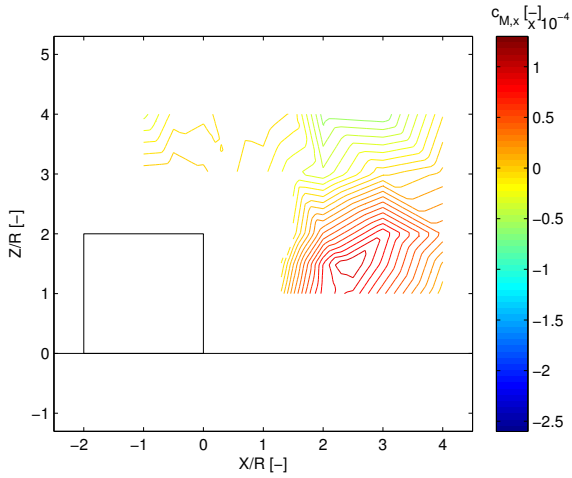

(c) x-moment coefficient

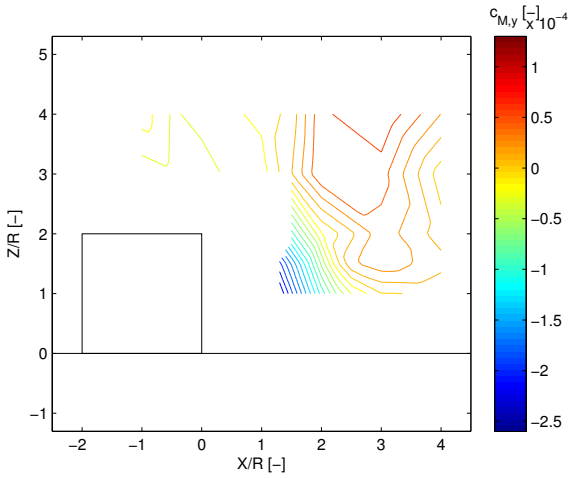

(d) y-moment coefficient

Fig. 4: Contours of the Loads acting on the rotor vs rotor position

stronger recirculation. In the other cases (further and closer to the obstacle) most of the air probably flows on the side of the obstacle instead of being redirected upwards. The effect of the obstacle start to be negligible when the rotor is further than 4 radia from the obstacle itself.

Another important feature of this region is the arising of strong pitching and rolling moments (up to 30% of the measured torque). This is due to the fact that the previously-introduced recirculation region mainly affects the portion of the rotor closer to the obstacle as it is shown in Figure 5e, where an increased induced velocity can be observed in the left portion of the inflow profile for $X/R = 3/2$. Consequently, a negative c_{My} moment is generated on the rotor, which is evident in Figure 3d and 4d for $Z/R = 3/2$ and $Z/R = 2$ close to the obstacle, which is equivalent to a pitching nose-down moment if a helicopter was facing the wall. It must be pointed out that, since we are dealing with a fixed rotor without flap and lag hinges, the blade dynamics is more similar to the one of a propeller than to the one of an fully-articulated rotor, implying that the the rotor responds without the typical 90 degrees lag. However a little lag is nevertheless present due to the blade flexibility, thus probably explaining the contextual presence in this region of a $x-$ moment in the plots of Figure 3c and 4c (even if with a much smaller value with respect to the $y-$moment).

For what concerns the torque measurements, very limited variations were observed among all the rotor positions (less than 2%), leading to a Figure of Merit behaviour (Figures 3b and 4b) that is very similar to the thrust coefficient one.

The in-plane velocity contours and streamlines are presented in Figure 6, in order to disclose the main features of the flow-field. As we can appreciate, the already introduced recirculation region is present in all the cases, even though its morphology is highly case-dependant. At $X/R = 3/2$ (Figures 6a, 6b, 6c) we can appreciate that the rotor slipstream

does not impinge on the floor before being deflected towards the obstacle, but impinges directly on the obstacle. This is due to the formation of a counter-rotating (with respect to the main one) recirculation region on the floor. This region is pushed towards the obstacle as the rotor is moved downwards. At $X/R = 2$ (Figures 6d, 6e, 6f), as already highlighted in the previous paragraphs, the rotor wake impinges on the floor before being deflected by the obstacle and re-ingested by the rotor. The air-layer that goes upwards close to the obstacle is thicker and faster than the other cases, probably indicating a stronger interaction with the rotor (confirmed, as previously stated, by the thrust measurements). Eventually at $X/R = 3$ (Figures 6g, 6h, 6i) the flow pattern is very similar to a non-disturbed rotor wake in ground effect, suggesting that the interaction in this case is weaker (as the load measurements confirm).

Eventually the out-of plane velocity component measurements are presented in Figure 7. As a convention, a positive out-of-plane velocity component corresponds to a vector pointing towards the reader. As we can appreciate the rotor slipstream is associated with a negative v, which is coherent with the fact that the left blade is entering the figure. Conversely the interface regions between the rotor slipstream and the recirculation regions on the ground and on the side of the obstacle are generally associated with a bland positive velocity, which means that in this region the air is going towards the reader. No particular variations of the out-of-plane velocity component are presented varying the rotor position.

CONCLUSIONS

In this paper a comprehensive experimental survey carried out at University of Glasgow is described, taking advantage of two different rotor rigs and several experimental techniques. Load measurements on the rotor were carried out in order to assess the rotor performance for different rotor positions with respect to a cubic obstacle, thus simulating a set of possible hovering flights around the obstacle. Laser Doppler Anemometry (LDA) measurements of the rotor inflow were used in order to see how the aerodynamic interaction affected the rotor performance. Eventually Particle Image Velocimetry (PIV) measurements in the region between the rotor and the obstacle were carried out in order to have a better insight of the interacting flow field.

The investigation showed two main regions of interest. The first region is the one above the edge of the obstacle, where the thrust coefficient decreases as the rotor is positioned outwards. In this case a gradual reduction of the inflow velocity is observed going from $X/R = 1$ to $X/R = -1$, as prescribed by the ground effect. Since only part of the rotor is over the obstacle, one would expect the inflow to be non-symmetrical. However, it results to be symmetrical leading to the generation of null pitch and roll moments.

The second region, probably of more interest, is the one just beside the obstacle ($1 < X/R < 2$, $1 < Z/R < 3$), where a recirculation region between the rotor and the obstacle develops. Its morphology is deeply dependent on the rotor position. This recirculation region implies a severe thrust loss (up to 8%)with respect to the one without obstacle at the same height. This thrust loss has a maximum at approximately 2 radia from the obstacle, whereas its influence appears to be negligible when the rotor is more than 4 radia away from the obstacle. Another important feature of this region is the arising of strong pitching and rolling moments (up to 30% of the measured torque), due to the non symmetrical inflow pattern on the rotor. Limited torque variations were observed throughout the testing (less than 2%), leading to the fact that the rotor figure of merit varied mostly according to the thrust coefficient.

Author contact:

Daniele Zagaglia	daniele.zagaglia@polimi.it;
Michea Giuni	michea.giuni@glasgow.ac.uk;
Richard Green	richard.green@glasgow.ac.uk

REFERENCES

[1]Zan, S., "On aerodynamic modelling and simulation of the dynamic interface," *Proceedings of the Institution of Mechanical Engineers, Part G: Journal of Aerospace Engineering*, Vol. 219, (5), 2005, pp. 393–410.

[2]Crozon, C., Steijl, R., and Barakos, G. N., "Numerical Study of Helicopter Rotors in a Ship Airwake," *Journal of Aircraft*, Vol. 51, (6), 2014, pp. 1813–1832.

[3]Kääriä, C. H., Wang, Y., Padfield, G. D., Forrest, J. S., and Owen, I., "Aerodynamic Loading Characteristics of a Model-Scale Helicopter in a Ship's Airwake," *Journal of Aircraft*, Vol. 49, (5), 2012, pp. 1271–1278.

[4]Lee, R. G. and Zan, S. J., "Wind tunnel testing of a helicopter fuselage and rotor in a ship airwake," *Journal of the American Helicopter Society*, Vol. 50, (4), 2005, pp. 326–337.

[5]Quinliven, T. and Long, K., "Rotor performance in the wake of a large structure," American Helicopter Society 65th Annual Forum, Grapewine, TX, May 2009.

[6]Rajagopalan, G., Niazi, S., Wadcock, A. J., Yamauchi, G. K., and Silva, M. J., "Experimental and Computational Study of the Interaction Between a Tandem-Rotor Helicopter and a Ship," American Helicopter Society 61st Annual Forum, Grapewine, TX, June 2005.

[7]Iboshi, N., Itoga, N., Prasad, J., and Sankar, L. N., "Ground Effect of a Rotor Hovering above a Confined Area," *Frontiers in Aerospace Engineering*, Vol. 3, (1), 2014.

[8]Gibertini, G., Grassi, D., Parolini, C., Zagaglia, D., and Zanotti, A., "Experimental investigation on the aerodynamic interaction between a helicopter and ground obstacles," *Proceedings of the Institution of Mechanical Engineers, Part G: Journal of Aerospace Engineering*, Vol. 229, (8), 2015, pp. 1395–1406.

[9]Prasad, A. K., "Stereoscopic particle image velocimetry," *Experiments in fluids*, Vol. 29, (2), 2000, pp. 103–116.

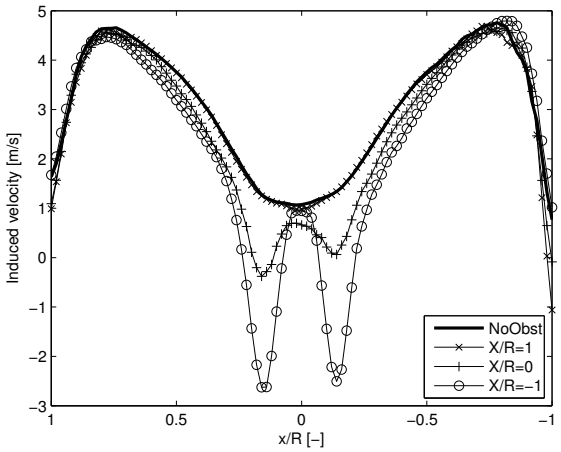

(a) $Z/R = 3$, Sweep in the x direction

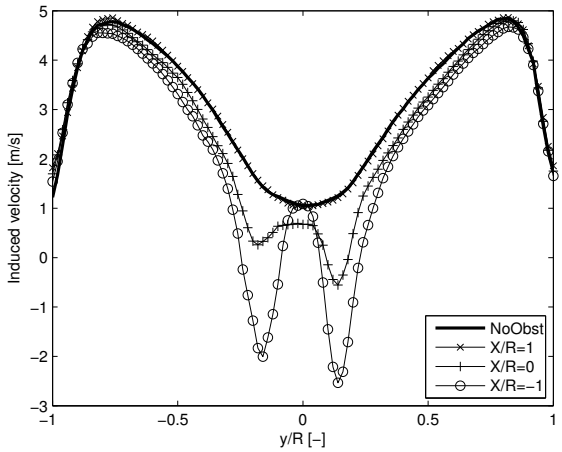

(b) $Z/R = 3$, Sweep in the y direction

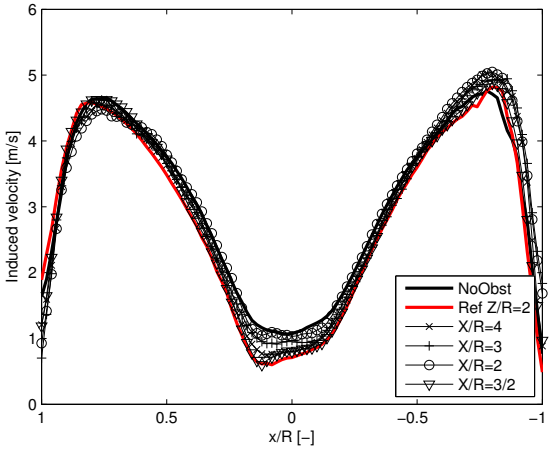

(c) $Z/R = 2$, Sweep in the x direction

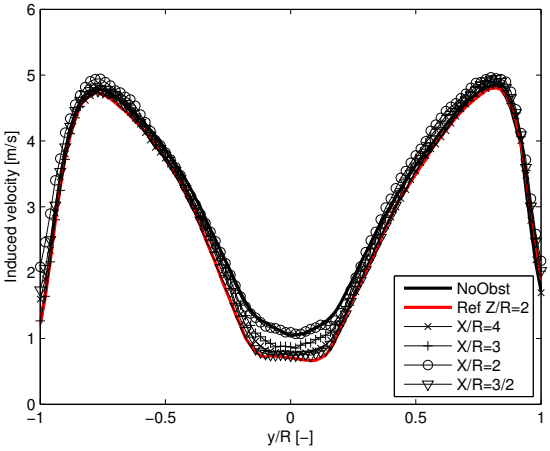

(d) $Z/R = 2$, Sweep in the y direction

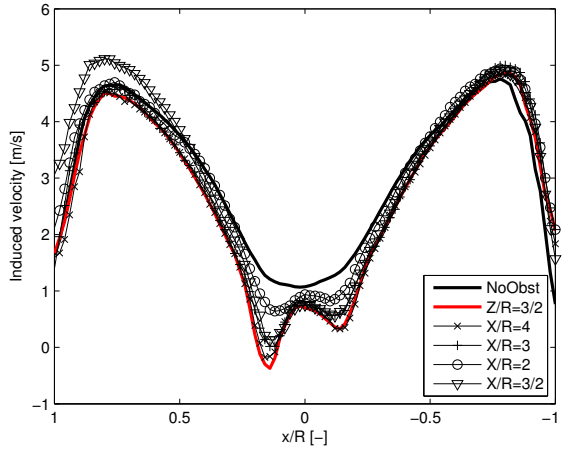

(e) $Z/R = 3/2$, Sweep in the x direction

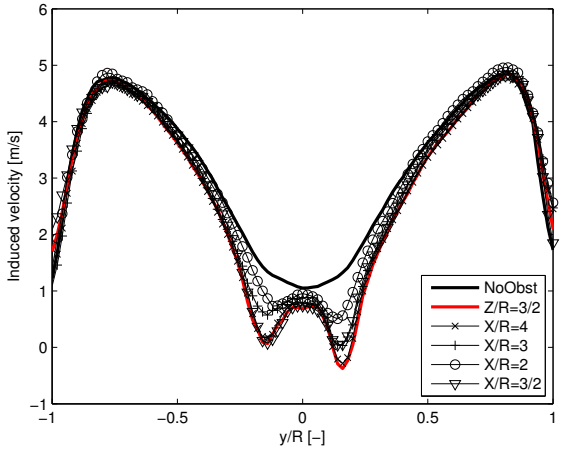

(f) $Z/R = 3/2$, Sweep in the y direction

Fig. 5: Induced velocity 4 cm above the rotor in the x (at $y/R = 0$) and y (at $x/R = 0$) directions. According to the convention of Fig 2, a positive induced velocity points downwards. The obstacle is on the left of the plots

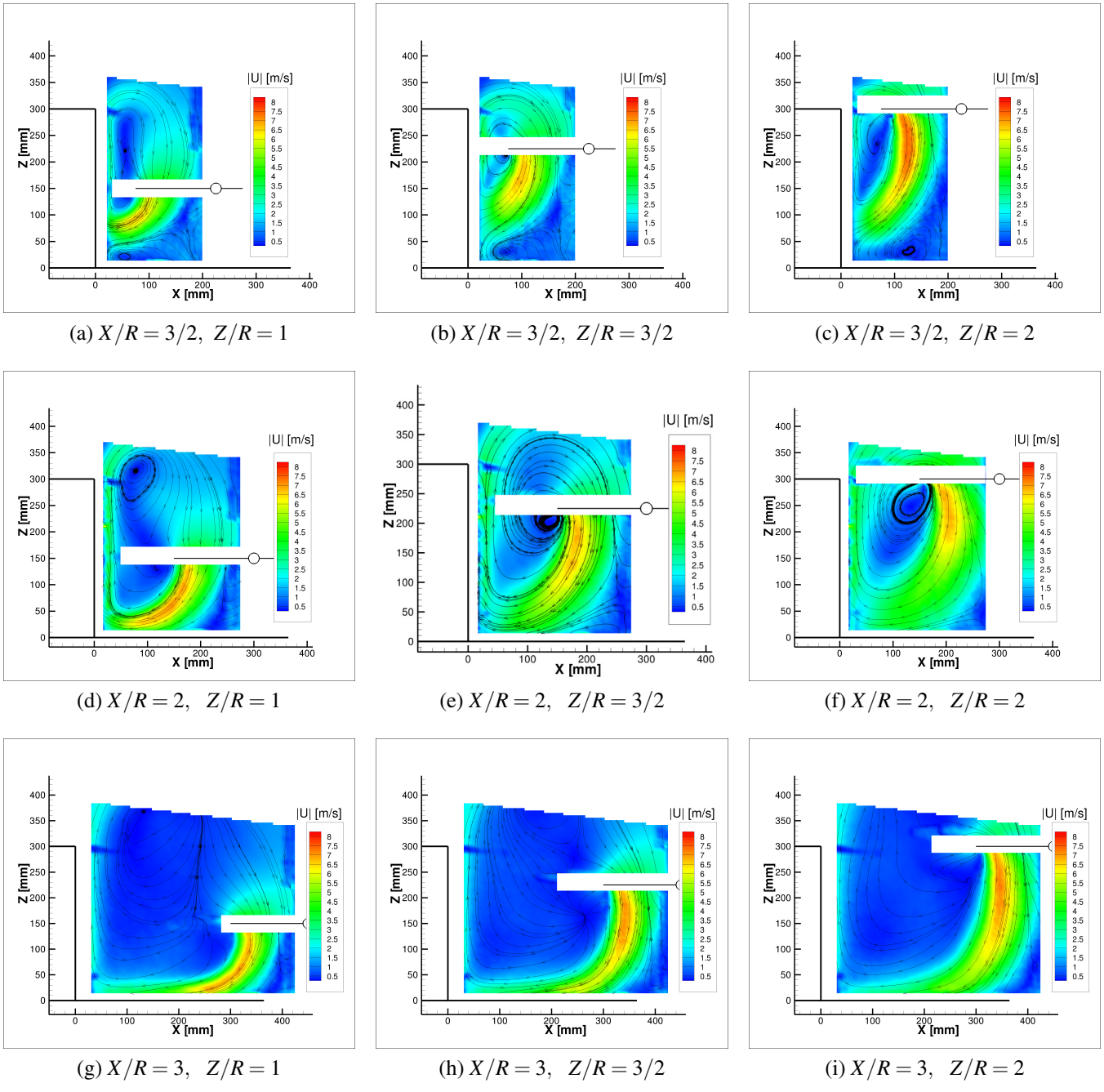

(a) $X/R = 3/2,\ Z/R = 1$ (b) $X/R = 3/2,\ Z/R = 3/2$ (c) $X/R = 3/2,\ Z/R = 2$

(d) $X/R = 2,\ Z/R = 1$ (e) $X/R = 2,\ Z/R = 3/2$ (f) $X/R = 2,\ Z/R = 2$

(g) $X/R = 3,\ Z/R = 1$ (h) $X/R = 3,\ Z/R = 3/2$ (i) $X/R = 3,\ Z/R = 2$

Fig. 6: PIV Measurments. In-plane velocity magnitude contours and In-plane streamlines in the problem symmetry plane ($Y/R = 0$) for different rotor positions with respect to the obstacle

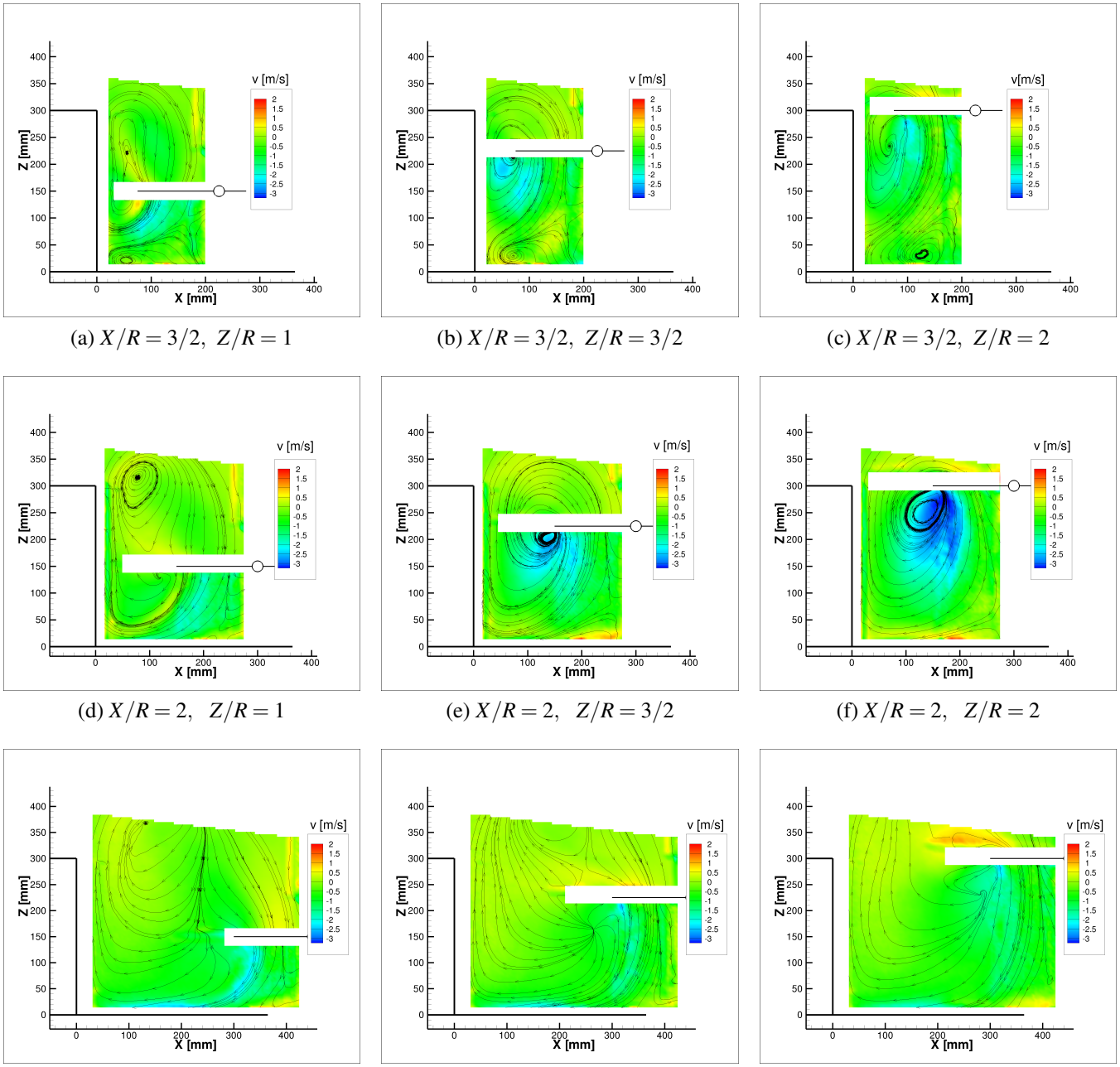

(a) $X/R = 3/2,\ Z/R = 1$ (b) $X/R = 3/2,\ Z/R = 3/2$ (c) $X/R = 3/2,\ Z/R = 2$

(d) $X/R = 2,\ Z/R = 1$ (e) $X/R = 2,\ Z/R = 3/2$ (f) $X/R = 2,\ Z/R = 2$

(g) $X/R = 3,\ Z/R = 1$ (h) $X/R = 3,\ Z/R = 3/2$ (i) $X/R = 3,\ Z/R = 2$

Fig. 7: PIV Measurments. Out-of-plane velocity contours and In-plane streamlines in the problem symmetry plane ($Y/R = 0$)for different rotor positions with respect to the obstacle. A positive velocity points towards the reader.